

A 1D shallow-flow model for two-layer flows based on FORCE scheme with wet-dry treatment

S. Martínez-Aranda^{1*}, A. Ramos-Pérez¹, P. García-Navarro¹,

¹Fluid Mechanics, University of Zaragoza, Spain

Abstract

The two-layer problem is defined as the coexistence of two immiscible fluids, separated by an interface surface. Under the shallow-flow hypothesis, 1D models are based on a 4 equations system accounting for the mass and momentum conservation in each fluid layer. Mathematically, the system of conservation laws modelling 1D two-layer flows has the important drawback of loss of hyperbolicity, causing that numerical schemes based on the eigenvalues of the Jacobian become unstable. In this work, well-balanced FORCE scheme is proposed for 1D two-layer shallow flows. The FORCE scheme combines the first-order Lax-Friedrichs flux and the second-order Lax-Wendroff flux. The scheme is supplemented with a hydrostatic reconstruction procedure in order to ensure the well-balanced behaviour of the model for steady flows even under wet-dry conditions. Additionally, a method to obtain high-accuracy numerical solutions for two-layer steady flows including friction dissipation is proposed to design reference benchmark tests for model validation. The enhanced FORCE scheme is faced to lake-at-rest benchmarking tests and steady flow cases including friction, demonstrating its well-balanced character. Furthermore, the numerical results obtained for highly unsteady two-layer dambreaks are used to analyze the robustness and accuracy of the model under a wide range of flow conditions.

Key words: Two-layer shallow flows, well-balanced FORCE scheme, hydrostatic reconstruction, wet-dry treatment, high-accuracy two-layer steady solutions.

*Corresponding author: sermar@unizar.com

1 Introduction

Some natural geophysical flows can be modelled as layered system consisting of two shallow fluids of distinct densities. The density ratio between the lighter upper layer and the heavier lower layer can be close to unity, as in stratified marine currents with different salinity, or extremely large as in the case of mine tailing dams. Under the hypothesis of two immiscible fluids where the vertical characteristic dimension of the flow is much smaller than their horizontal extension, these kind of geophysical flows have been often modelled using the depth-averaged shallow-flow equations in both layers and involving a free surface [1–3].

When considering flow per unit width, the 1D two-layer shallow-flow problem, from the mathematical point of view, consists of a system of 4 conservation laws involving mass and momentum conservation for each layer. It has been studied by a considerable amount of researchers [4–7], not only because of its applications but also because of the mathematical challenge itself. The two-layer system is conditionally hyperbolic and stable. Both layers interact by means of the hydrostatic pressure terms caused by the slope of both the free surface and the internal interface separating the two fluids, as well as by the momentum exchange at the interface due to friction.

One of the main features of the two-layer shallow-flow system is the loss of hyperbolicity which arises under a wide range of flow conditions [4, 5]. The appearance of this complex behaviour is related to the density ratio between fluids and the velocity difference between layers [2]. This conditionally non-hyperbolic character of the two-layer shallow flow system has given rise to an extensive list of proposed solutions in order to avoid the appearance of numerical instabilities [1, 3, 6–10]. Traditionally, numerical schemes based on the computation of the two-layer system eigenvalues, such as the HLLC or the A-Roe schemes, have failed in the treatment of the loss of hyperbolicity and avoiding the appearance of numerical instabilities. Furthermore, many of the reported numerical schemes for two-layer or multi-layer

systems are complex to implement as the numerical scheme usually includes a specific method to deal with those instabilities. For instance [9] solves the problem introducing a term associated with the fluids compressibility which manages the instabilities changing the density of the layers; in addition, an interface artificial turbulence is added to increase diffusivity. The use of an entropy satisfying scheme [7] or an optimal amount of friction in a corrector step [3] which keeps the flow inside the hyperbolic region has also been proposed.

The list of authors who have addressed the problem from the analytical point of view is much shorter [11, 12]. In the case of [12], the solutions are restricted to the rigid-lid assumption (a uniform free surface) to similar density of both layers, smooth bed functions and frictionless conditions. Up to now, the validation of new two-layer numerical schemes relies on a few analytic solution for specific cases which, in general, do not include friction. In [13], a two-layer shallow flow model based on Roe-scheme including friction terms is validated using a salt-wedge case with a steady reference solution obtained from the ODE system previously proposed by [14].

This article presents a new 1D FORCE scheme [15] for the two-layer shallow-flow equations, including friction source terms. A hydrostatic reconstruction procedure is also proposed to ensure the well-balanced behaviour of the scheme under steady flow conditions involving source terms. Furthermore, in order to design reference benchmark tests for two-layer models validation, a method to obtain high-accuracy numerical solutions for two-layer steady flows including friction dissipation is also proposed, based on the single-layer method reported by [16]. The proposed scheme is faced to lake-at-rest, steady and transient flow benchmarking tests, proving its well-balanced character, robustness and accuracy under a wide range of fluid characteristic and flow conditions.

The text is organised as follows: in Section 2 the two-layer governing equations are stated, including the coupling pressure terms between layers and the friction source terms; Section 3 is devoted to the proposed well-balanced FORCE scheme

supplemented with the hydrostatic reconstruction; in Section 4, the new procedure to obtain high-accuracy numerical solutions for two-layer steady problems is presented.

60 The numerical results obtained with the proposed scheme for different steady and transient benchmarking tests are presented in Section 5. Finally, the conclusion of this work have been drawn in Section 6.

2 Mathematical model and governing equations

The one-dimensional two-layer shallow water equations result from depth integration 65 of the 3D incompressible Navier-Stokes mass and momentum equations, according to the scheme shown in Figure 1. The lower layer, referred to as layer 2, is integrated between the bed surface z_b and the interphase surface z_w , whereas the upper layer, referred as layer 1, is integrated between the interphase surface z_w and the free surface z_s . Considering a density ratio $r = \rho_1/\rho_2$, being ρ_1 the density of the lighter upper layer 1 and ρ_2 the density of the heavier lower layer 2, the following system of 70 partial differential equations can be obtained for the two-layer flow per unit width:

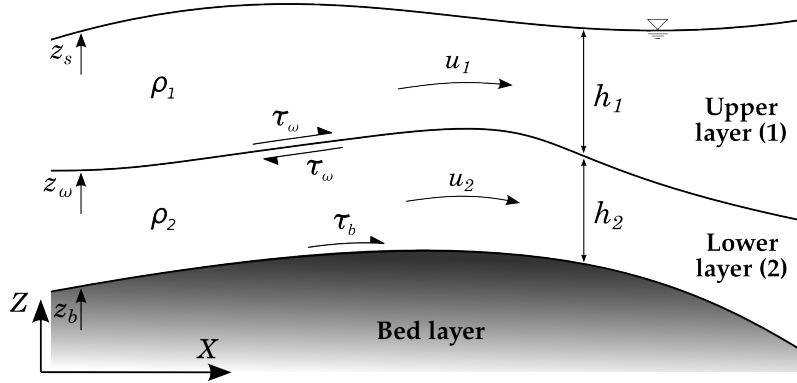


Figure 1: Scheme for 1D two-layer shallow-flow problem.

$$\begin{aligned}
 \frac{\partial}{\partial t}(h_1) + \frac{\partial}{\partial x}(h_1 u_1) &= 0 \\
 \frac{\partial}{\partial t}(h_1 u_1) + \frac{\partial}{\partial x}(h_1 u_1^2 + g \frac{1}{2} h_1^2) &= -g h_1 \frac{\partial z_b}{\partial x} - P_1 - \frac{\tau_w}{\rho_1} \\
 \frac{\partial}{\partial t}(h_2) + \frac{\partial}{\partial x}(h_2 u_2) &= 0 \\
 \frac{\partial}{\partial t}(h_2 u_2) + \frac{\partial}{\partial x}(h_2 u_2^2 + g \frac{1}{2} h_2^2) &= -g h_2 \frac{\partial z_b}{\partial x} - P_2 + \frac{\tau_w}{\rho_2} - \frac{\tau_b}{\rho_2}
 \end{aligned} \tag{1}$$

where g [LT^{-2}] is the acceleration of gravity, h_1 , h_2 [L] are the layer depths, u_1 , u_2 [LT^{-1}] are the depth-averaged velocities of each layer in the x direction and z_b [L] is the fixed bottom level. The boundary shear stresses τ_w [$ML^{-1}T^{-2}$] and τ_b [$ML^{-1}T^{-2}$] are those acting at the interface surface between fluid layers and at the fixed bottom. The pressure coupling terms P_1 [L^2T^{-2}] and P_2 [L^2T^{-2}] between both layers are expressed as:

$$\begin{aligned} \text{Upper layer: } P_1 &= gh_1 \frac{\partial h_2}{\partial x} \\ \text{Lower layer: } P_2 &= rgh_2 \frac{\partial h_1}{\partial x} \end{aligned} \quad (2)$$

and they appear as a results of the vertical averaging of the three-dimensional problem [17], transforming the system in an non-homogeneous problem even in cases over frictionless surfaces and flat bottom. Those terms characterize the two-layer flow equations as they describe the pressure momentum exchange between layers, i.e. P_2 accounts for the hydrostatic pressure of the upper layer 1 on the lower layer 2 and P_1 considers the interface surface slope, which is equivalent to a bed slope term for the upper layer 1.

There is a formal analogy with the 1D single-layer shallow water flow [7]. The main difference is that the coupling terms, P_2 and P_1 , are not fixed but also time-dependent. These source terms make the double-layer shallow water a complex flow to simulate numerically. It can easily lead to strong instabilities associated with physical phenomena as layers mixing and shear flows [8].

The boundary shear stress between the lower layer and the fixed bed τ_b , assuming a turbulent flow for the lower layer, is defined with the squared flow velocity [18]:

$$\tau_b = \rho_2 g h_2 C_{fb} u_2 |u_2| \quad (3)$$

being C_{fb} the friction turbulent factor, according to the Manning's law [19] it is defined as $C_{fb} = n_b^2 / h_2^{4/3}$, where n_b is the bed roughness coefficient. The interface friction term is Chézy-type [20], depending on the square of the relative velocity between the upper and the lower layer:

$$\tau_\omega = \rho_1 g C_{f\omega,1} (u_1 - u_2) |u_1 - u_2| = \rho_2 g C_{f\omega,2} (u_1 - u_2) |u_1 - u_2| \quad (4)$$

being $C_{f\omega,2} = r C_{f\omega,1}$ and $C_{f\omega,1}$ the interface friction coefficients for the lower layer and the upper layers, respectively.

The 1D system (1) can be reordered in vector form as:

$$\frac{\partial \mathbf{U}}{\partial t} + \frac{\partial \mathbf{F}(\mathbf{U})}{\partial x} = \mathbf{S}(\mathbf{U}) \quad (5)$$

where \mathbf{U} is the conserved variables vector and $\mathbf{F}(\mathbf{U})$ is the convective flux vector:

$$\mathbf{U} = \begin{pmatrix} h_1 \\ h_1 u_1 \\ h_2 \\ h_2 u_2 \end{pmatrix} \quad \mathbf{F}(\mathbf{U}) = \begin{pmatrix} h_1 u_1 \\ h_1 u_1^2 + \frac{1}{2} g h_1^2 \\ h_2 u_2 \\ h_2 u_2^2 + \frac{1}{2} g h_2^2 \end{pmatrix} \quad (6)$$

100 The source vector $\mathbf{S}(\mathbf{U})$ includes the bottom slope, the friction stress terms at the fixed bed surface, the boundary shear stress at the interface boundary, as well as the pressure coupling terms P_1 and P_2 between both layers:

$$\mathbf{S}(\mathbf{U}) = \begin{pmatrix} 0 \\ -g h_1 \frac{\partial z_b}{\partial x} - P_1 - \frac{\tau_\omega}{\rho_1} \\ 0 \\ -g h_2 \frac{\partial z_b}{\partial x} - P_2 + \frac{\tau_\omega}{\rho_2} - \frac{\tau_b}{\rho_2} \end{pmatrix} \quad (7)$$

This kind of formulation for the two-layer problem is referred to as the uncoupled formulation, since all the coupling terms between layers, i.e. P_2 and P_1 , are included
105 in the source vector \mathbf{S} [2]. The Jacobian matrix of the convective fluxes is defined as $\mathbf{J}(\mathbf{U}) = \frac{\partial \mathbf{F}}{\partial \mathbf{U}}$ leading to the following quasi-linear partial derivative system:

$$\frac{\partial \mathbf{U}}{\partial t} + \mathbf{J}(\mathbf{U}) \frac{\partial \mathbf{U}}{\partial x} = \mathbf{S}(\mathbf{U}) \quad (8)$$

with:

$$\mathbf{J}(\mathbf{U}) = \begin{pmatrix} 0 & 1 & 0 & 0 \\ c_1^2 - u_1^2 & 2u_1 & 0 & 0 \\ 0 & 0 & 0 & 1 \\ 0 & 0 & c_2^2 - u_2^2 & 2u_2 \end{pmatrix} \quad (9)$$

being $c_1 = \sqrt{gh_1}$ and $c_2 = \sqrt{gh_2}$ the infinitesimal wave celerities in the upper and lower layer, respectively. The Jacobian matrix $\mathbf{J}(\mathbf{U})$ has four different real
 110 eigenvalues:

$$\begin{aligned} \lambda_I &= u_1 - c_1 \\ \lambda_{II} &= u_1 + c_1 \\ \lambda_{III} &= u_2 - c_2 \\ \lambda_{IV} &= u_2 + c_2 \end{aligned} \quad (10)$$

The eigenvalues, λ_I y λ_{II} in (10) are related to the upper layer whereas λ_{III} and λ_{IV} are associated to the bottom layer. They are considered to control the numerical stability of explicit schemes through the CFL condition. If the convective fluxes vector $\mathbf{F}(\mathbf{U})$ is defined including the coupling terms P_2 and P_1 , leading to the
 115 coupled formulation of the two-layer problem, the eigenvalues of the Jacobian are not explicit [3, 8] and can only be approximated when the density ratio $r = \rho_1/\rho_2 \approx 1$. Closed-form solutions for eigenvalues of the coupled Jacobian matrix have been recently presented in [21] and tested in [22]. Furthermore, this coupled formulation which includes the pressure terms P_2 and P_1 into the convective fluxes, in order to
 120 concentrate in the Jacobian of the system all the relevant information, might lead to the loss of the hyperbolic character of the system (5) in a wide range of flow regimes [2].

3 FORCE numerical method for two-layer systems with source terms

125 The FORCE scheme [15, 23–25] is an explicit centered finite volume method (FVM) with proved numerical stability and robustness. For the sake of simplicity, a uniform spatial Δx and variable temporal Δt discretization (Figure 2) is applied to solve the two-layer shallow water flow equations (1), which are integrated spatially and temporally as follows:

$$\int_{x_{i-\frac{1}{2}}}^{x_{i+\frac{1}{2}}} [\mathbf{U}(x, t_{n+1}) - \mathbf{U}(x, t_n)] dx = \int_{t_n}^{t_{n+1}} \left(\mathbf{F}_{i-\frac{1}{2}} - \mathbf{F}_{i+\frac{1}{2}} \right) dt + \int_{t_n}^{t_{n+1}} \int_{x_{i-\frac{1}{2}}}^{x_{i+\frac{1}{2}}} \mathbf{S}(\mathbf{U}(x, t)) dx dt \quad (11)$$

130 where the convective fluxes $\mathbf{F}_{i-\frac{1}{2}}$ and $\mathbf{F}_{i+\frac{1}{2}}$ are defined as:

$$\begin{aligned} \mathbf{F}_{i-\frac{1}{2}} &= \mathbf{F} \left(\mathbf{U}(x_{i-\frac{1}{2}}, t) \right) \\ \mathbf{F}_{i+\frac{1}{2}} &= \mathbf{F} \left(\mathbf{U}(x_{i+\frac{1}{2}}, t) \right) \end{aligned} \quad (12)$$

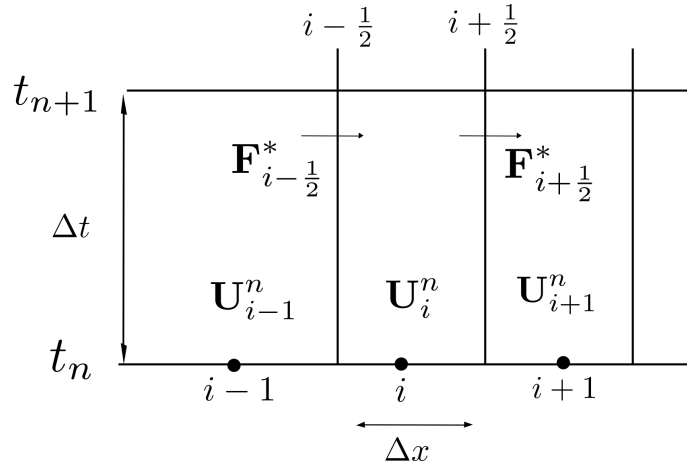


Figure 2: FVM sketch for two-layer FORCE scheme.

Assuming a piecewise constant representation for the conserved variables \mathbf{U}_i^n at the i cell for the time level n as:

$$U_i^n = \frac{1}{\Delta x} \int_{x_{i-\frac{1}{2}}}^{x_{i+\frac{1}{2}}} U(x, t_n) dx \quad (13)$$

it is possible to define the numerical flux $\mathbf{F}_{i+\frac{1}{2}}^*$ at the $i + \frac{1}{2}$ intercell edge separating cells i and $i + 1$ as:

$$\mathbf{F}_{i+\frac{1}{2}}^* = \frac{1}{\Delta t} \int_{t_n}^{t_{n+1}} \mathbf{F} \left(U(x_{i+\frac{1}{2}}, t) \right) dt \quad (14)$$

135 Therefore, the 1D scheme for the conserved variables updating at the i cell can be expressed as:

$$U_i^{n+1} = U_i^n - \frac{\Delta t}{\Delta x} (\mathbf{F}_{i+\frac{1}{2}}^* - \mathbf{F}_{i-\frac{1}{2}}^*) + \frac{\Delta t}{\Delta x} \mathbf{S}_i^* \quad (15)$$

where Δt is the time step and Δx is the cell size. The source contribution, including bed slope, pressure and shear stress components, is approximated using an spatially integrated term \mathbf{S}_i^* defined as follows:

$$\Delta t \mathbf{S}_i^* \approx \Delta t \int_{x_{i-\frac{1}{2}}}^{x_{i+\frac{1}{2}}} \mathbf{S}(U(x, t^n)) dx \approx \int_{t_n}^{t_{n+1}} \int_{x_{i-\frac{1}{2}}}^{x_{i+\frac{1}{2}}} \mathbf{S}(U(x, t)) dx dt \quad (16)$$

140 The FORCE numerical flux at the intercell edges is formulated in a single step as a combination of the Lax-Friedrichs (first order and highly diffusive) [26] and the Lax-Wendroff (second order and conditionally oscillatory) [27] fluxes:

$$\mathbf{F}_{i+\frac{1}{2}}^* = \alpha \mathbf{F}_{i+\frac{1}{2}}^{LF} + (1 - \alpha) \mathbf{F}_{i+\frac{1}{2}}^{LW} \quad (17)$$

where $0 \leq \alpha \leq 1$ is a weighting parameter, $\mathbf{F}_{i+\frac{1}{2}}^{LF}$ is the Lax-Friedrichs flux at the intercell edge $i + \frac{1}{2}$, computed as:

$$\mathbf{F}_{i+\frac{1}{2}}^{LF} = \frac{1}{2} \left[\mathbf{F}(U_{i+\frac{1}{2}}^-) + \mathbf{F}(U_{i+\frac{1}{2}}^+) \right] - \frac{1}{2} \frac{\Delta x}{\Delta t} (U_{i+\frac{1}{2}}^+ - U_{i+\frac{1}{2}}^-) \quad (18)$$

145 and $\mathbf{F}_{i+\frac{1}{2}}^{LW}$ is the Lax-Wendroff numerical fluxes at the intercell edge $i + \frac{1}{2}$, computed

as:

$$\begin{aligned}\mathbf{F}_{i+\frac{1}{2}}^{LW} &= \mathbf{F}(\mathbf{U}_{i+\frac{1}{2}}^{LW}) \\ \mathbf{U}_{i+\frac{1}{2}}^{LW} &= \frac{1}{2}(\mathbf{U}_{i+\frac{1}{2}}^- + \mathbf{U}_{i+\frac{1}{2}}^+) - \frac{1}{2} \frac{\Delta t}{\Delta x} \left[\mathbf{F}(\mathbf{U}_{i+\frac{1}{2}}^+) - \mathbf{F}(\mathbf{U}_{i+\frac{1}{2}}^-) \right]\end{aligned}\tag{19}$$

being $\mathbf{U}_{i+\frac{1}{2}}^-$ and $\mathbf{U}_{i+\frac{1}{2}}^+$ the set of conserved variables provided by the hydrostatic reconstruction (see Section 3.1) at the left and right side of the intercell edge $i + \frac{1}{2}$, respectively.

150 The spatial integration of the source terms vector at the cell i , \mathbf{S}_i^* , is approximated as:

$$\mathbf{S}_i^* = \begin{pmatrix} 0 \\ -\tilde{S}_{p1} - \frac{\tilde{T}_\omega}{\rho_1} \\ 0 \\ -\tilde{S}_{p2} + \frac{\tilde{T}_\omega}{\rho_2} - \frac{\tilde{T}_b}{\rho_2} \end{pmatrix}_i \tag{20}$$

where $\tilde{S}_{p1,i}$ and $\tilde{S}_{p2,i}$ account for the integrated pressure forces at the upper and lower layers of cell i , respectively; and $\tilde{T}_{b,i} = \tau_b(\mathbf{U}_i^n) \Delta x$ and $\tilde{T}_{\omega,i} = \tau_\omega(\mathbf{U}_i^n) \Delta x$ are the integrated friction forces at the bed and interface surfaces along cell i , respectively.

155 The terms $\tilde{S}_{p1,i}$ and $\tilde{S}_{p2,i}$ are computed as:

$$\begin{aligned}\tilde{S}_{p1,i} &= (g\tilde{h}_1 \Delta z_b + \tilde{P}_1 \Delta x)_i = (g\tilde{h}_1 \Delta(z_b + h_2))_i = (g\tilde{h}_1 \Delta\xi_1)_i \\ \tilde{S}_{p2,i} &= (g\tilde{h}_2 \Delta z_b + \tilde{P}_2 \Delta x)_i = (g\tilde{h}_2 \Delta(z_b + rh_1))_i = (g\tilde{h}_2 \Delta\xi_2)_i\end{aligned}\tag{21}$$

defining the virtual pressure surface for the upper and lower layers, ξ_1 and ξ_2 respectively, as:

$$\xi_1 = z_b + h_2 \qquad \xi_2 = z_b + rh_1 \tag{22}$$

The values for the virtual pressure surface variation $\Delta\xi_{1,i}$ and $\Delta\xi_{2,i}$, and the

averaged layer depth $\tilde{h}_{1,i}$ and $\tilde{h}_{i,2}$ at cell i are provided by the hydrostatic reconstruction for the upper and lower layers. This reconstruction has been designed to ensure a well-balanced equilibrium of the fluxes at the intercell edges under static equilibrium conditions, as well as the correct treatment of the wet-dry fronts for both layers (see Section 3.1).

Furthermore, the explicit FORCE scheme requires a time step Δt limitation to ensure the numerical stability of the method:

$$\Delta t = \text{CFL} \frac{\Delta x}{\lambda_k^{max}} \quad (23)$$

being the eigenvalue λ_k^{max} the maximum of all the eigenvalues over the domain at every time and $\text{CFL} \leq 1$ the Courant-Friedrichs-Lewy [28] condition.

3.1 Well-balanced hydrostatic reconstruction

The original FORCE scheme [15] was proposed for homogeneous systems, but including source terms into an enhanced formulation requires a careful treatment in order to ensure the well-balance property of the numerical scheme when dealing with flow steady states. The well-balanced FORCE version proposed here, which balances the source terms integral with the intercell numerical fluxes, uses the hydrostatic reconstruction method [29, 30] as well as a correct treatment of the wet-dry front for both layers.

The main idea is to formulate the discrete source term at cell i and the numerical fluxes at the intercell edges $i - \frac{1}{2}$ and $i + \frac{1}{2}$ to achieve the balance between the convective fluxes and the source terms during the time step:

$$\mathbf{F}_{i+\frac{1}{2}}^* - \mathbf{F}_{i-\frac{1}{2}}^* - \mathbf{S}_i^* = 0 \quad (24)$$

The condition (24) requires to reconstruct the discrete values of the set of conserved variables at the left and right sides of the $i + \frac{1}{2}$ intercell edge, $\mathbf{U}_{i+\frac{1}{2}}^-$ and $\mathbf{U}_{i+\frac{1}{2}}^+$ respectively. Moreover, it is necessary to define the degrees of freedom on the

integrated source term \mathbf{S}_i^* (20), i.e. the virtual pressure surface variations ($\Delta\xi_{1,i}$, $\Delta\xi_{2,i}$) and the averaged depth ($\tilde{h}_{1,i}$ and $\tilde{h}_{i,2}$).

There exist two different conditions which require the maintenance of the static equilibrium state. First, under null velocity and horizontal free surface level conditions, $z_{s,i} = z_{s,i+1}$, the solution must remain in equilibrium if the density of both layers is equal, i.e. $r = 1/1$, regardless of the position of the interface surface z_ω (Figure 3-a). Second, under null velocity and horizontal free and interface surfaces, $z_{s,i} = z_{s,i+1}$ and $z_{\omega,i} = z_{\omega,i+1}$, the static equilibrium must remain unaltered for any value of the density ratio r (Figure 3-b). The proposed hydrostatic reconstruction method is based on the proper definition of the virtual pressure surfaces ξ_1 and ξ_2 , as well as the virtual free surfaces η_1 and η_2 , for both the upper and the lower layers respectively.

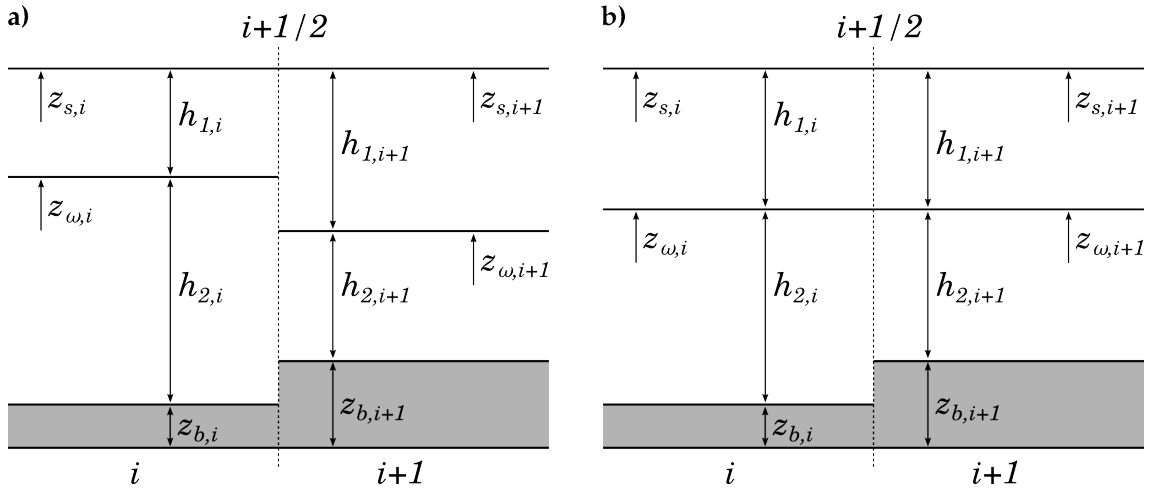


Figure 3: Hydrostatic equilibrium conditions: a) static equilibrium with density ratio $r = 1/1$ and b) static equilibrium with horizontal free and interface surfaces.

For the upper layer, the virtual pressure surface ξ_1 at cells i and $i + 1$ is defined

as:

$$\begin{aligned}\xi_{1,i} &= z_{b,i} + h_{2,i} \\ \xi_{1,i+1} &= z_{b,i+1} + h_{2,i+1}\end{aligned}\tag{25}$$

and the virtual free surface η_1 at cells i and $i + 1$ is can be expressed as:

$$\eta_{1,i} = \xi_{1,i} + h_{1,i} \quad (26)$$

$$\eta_{1,i+1} = \xi_{1,i+1} + h_{1,i+1}$$

which agree with the physical interface surface z_ω and the physical free surface z_s respectively (Figure 4). The average value of the virtual pressure surface for the upper layer at the edge $\xi_{1,i+\frac{1}{2}}$ can be computed as:

$$\xi_{1,i+\frac{1}{2}} = \frac{1}{2}(\xi_{1,i} + \xi_{1,i+1}) \quad (27)$$

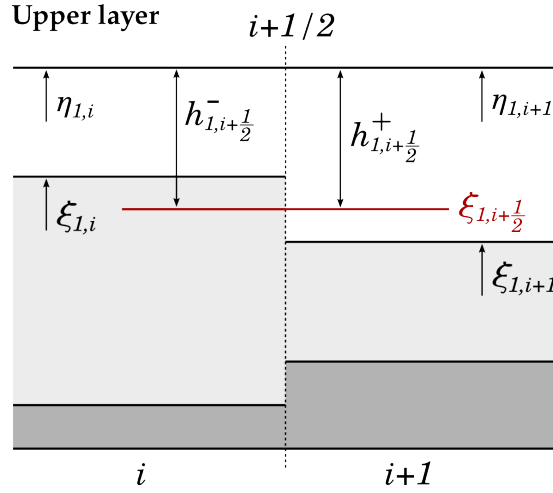


Figure 4: Hydrostatic reconstruction of the upper layer under equilibrium condition.

200 The first component of the reconstructed conserved variables $\mathbf{U}_{i+\frac{1}{2}}^-$ and $\mathbf{U}_{i+\frac{1}{2}}^+$, i.e. the upper layer depth, is defined as:

$$\begin{aligned} h_{1,i+\frac{1}{2}}^- &= \eta_{1,i} - \xi_{1,i+\frac{1}{2}} \\ h_{1,i+\frac{1}{2}}^+ &= \eta_{1,i+1} - \xi_{1,i+\frac{1}{2}} \end{aligned} \quad (28)$$

From this, the second component of the reconstructed conserved variables at the intercell edge $i + \frac{1}{2}$, associated with the upper layer discharge, is defined as:

$$\begin{aligned}
(hu)_{1,i+\frac{1}{2}}^- &= h_{1,i+\frac{1}{2}}^- u_{1,i} \\
(hu)_{1,i+\frac{1}{2}}^+ &= h_{1,i+\frac{1}{2}}^+ u_{1,i+1}
\end{aligned} \tag{29}$$

being $u_{1,i}$ and $u_{1,i+1}$ the upper layer velocities at cells i and $i+1$, respectively. Under
205 hydrostatic equilibrium, $(hu)_{1,i+\frac{1}{2}}^- = (hu)_{1,i+\frac{1}{2}}^+ = 0$ and there exists a constant free
surface $\eta_{1,i} = \eta_{1,i+1}$ for both configurations depicted in Figure 3. Therefore, in this
case $h_{1,i+\frac{1}{2}}^- = h_{1,i+\frac{1}{2}}^+$. Replacing in (24), the homogeneous numerical fluxes balance
at cell i for the upper layer can be expressed as:

$$\mathbf{F}_{1,i+\frac{1}{2}}^* - \mathbf{F}_{1,i-\frac{1}{2}}^* = \begin{pmatrix} 0 \\ \frac{1}{2}g \left[(h_{1,i+\frac{1}{2}}^-)^2 - (h_{1,i-\frac{1}{2}}^+)^2 \right] \end{pmatrix} \tag{30}$$

Therefore, to ensure the static equilibrium, the averaged depth $\tilde{h}_{1,i}$ and the
210 virtual pressure surface variation $\Delta\xi_{1,i}$ present in the pressure force term $\tilde{S}_{p1,i}$ for
the upper layer at cell i (21) should be defined as:

$$\begin{aligned}
\tilde{h}_{1,i} &= \frac{1}{2}(h_{1,i+\frac{1}{2}}^- + h_{1,i-\frac{1}{2}}^+) \\
\Delta\xi_{1,i} &= \xi_{1,i+\frac{1}{2}} - \xi_{1,i-\frac{1}{2}} = h_{1,i-\frac{1}{2}}^+ - h_{1,i+\frac{1}{2}}^-
\end{aligned} \tag{31}$$

and hence $\mathbf{F}_{1,i+\frac{1}{2}}^* - \mathbf{F}_{1,i-\frac{1}{2}}^* = \mathbf{S}_{1,i}^*$.

Analogously, for the lower layer, the virtual pressure surface ξ_2 at cells i and $i+1$
is:

$$\begin{aligned}
\xi_{2,i} &= z_{b,i} + rh_{1,i} \\
\xi_{2,i+1} &= z_{b,i+1} + rh_{1,i+1}
\end{aligned} \tag{32}$$

215 and the virtual free surface η_2 at cells i and $i+1$ is:

$$\begin{aligned}\eta_{2,i} &= \xi_{2,i} + h_{2,i} \\ \eta_{2,i+1} &= \xi_{2,i+1} + h_{2,i+1}\end{aligned}\tag{33}$$

The reconstruction scheme focusing on the lower layer is depicted in Figure 5. Note that the effect of the upper layer is included into the virtual pressure surface. The average value of the virtual pressure surface for the lower layer at the edge $\xi_{2,i+\frac{1}{2}}$ can be computed as:

$$\xi_{2,i+\frac{1}{2}} = \frac{1}{2}(\xi_{2,i} + \xi_{2,i+1})\tag{34}$$

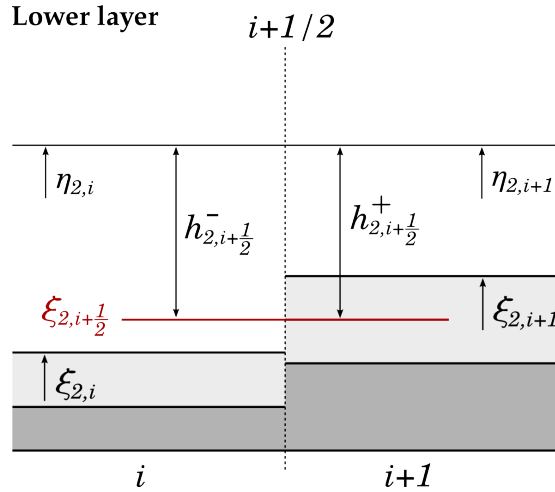


Figure 5: Hydrostatic reconstruction of the lower layer under equilibrium condition.

220 The third component of the reconstructed conserved variables $\mathbf{U}_{i+\frac{1}{2}}^-$ and $\mathbf{U}_{i+\frac{1}{2}}^+$, depth the lower layer depth, is defined as:

$$\begin{aligned}h_{2,i+\frac{1}{2}}^- &= \eta_{2,i} - \xi_{2,i+\frac{1}{2}} \\ h_{2,i+\frac{1}{2}}^+ &= \eta_{2,i+1} - \xi_{2,i+\frac{1}{2}}\end{aligned}\tag{35}$$

From this, the fourth component of the reconstructed conserved variables at the intercell edge $i + \frac{1}{2}$, associated with the lower layer discharge, is:

$$\begin{aligned}
(hu)_{2,i+\frac{1}{2}}^- &= h_{2,i+\frac{1}{2}}^- u_{2,i} \\
(hu)_{2,i+\frac{1}{2}}^+ &= h_{2,i+\frac{1}{2}}^+ u_{2,i+1}
\end{aligned} \tag{36}$$

being $u_{2,i}$ and $u_{2,i+1}$ the lower layer velocities at cells i and $i+1$, respectively. Under
225 hydrostatic equilibrium, $(hu)_{2,i+\frac{1}{2}}^- = (hu)_{2,i+\frac{1}{2}}^+ = 0$ and the virtual free surface for
the lower layer is constant $\eta_{2,i} = \eta_{2,i+1}$ for both equilibrium configurations depicted
in Figure 3, hence also for the lower layer $h_{2,i+\frac{1}{2}}^- = h_{2,i+\frac{1}{2}}^+$.

Following the same procedure as for the upper layer, the averaged depth $\tilde{h}_{2,i}$ and
the virtual pressure surface variation $\Delta\xi_{2,i}$ present in the pressure force term $\tilde{S}_{p2,i}$
230 for the lower layer at cell i (21) should be defined as:

$$\begin{aligned}
\tilde{h}_{2,i} &= \frac{1}{2}(h_{2,i+\frac{1}{2}}^- + h_{2,i-\frac{1}{2}}^+) \\
\Delta\xi_{2,i} &= \xi_{2,i+\frac{1}{2}} - \xi_{2,i-\frac{1}{2}} = h_{2,i-\frac{1}{2}}^+ - h_{2,i+\frac{1}{2}}^-
\end{aligned} \tag{37}$$

and hence $\mathbf{F}_{2,i+\frac{1}{2}}^* - \mathbf{F}_{2,i-\frac{1}{2}}^* = \mathbf{S}_{2,i}^*$.

3.2 Wet-dry fronts treatment

In order to ensure a correct treatment of the wet-dry fronts in both layers, the pres-
sure force source term $\tilde{S}_{p1,i}$ and $\tilde{S}_{p2,i}$ at the upper and lower layer (21), respectively,
235 can be decomposed as:

$$\begin{aligned}
\tilde{S}_{p1,i} &= \tilde{S}_{p1,i-\frac{1}{2}}^+ + \tilde{S}_{p1,i+\frac{1}{2}}^- = \left[\frac{1}{2}g(h_{1,i-\frac{1}{2}}^+)^2 \right] + \left[-\frac{1}{2}g(h_{1,i+\frac{1}{2}}^-)^2 \right] \\
\tilde{S}_{p2,i} &= \tilde{S}_{p2,i-\frac{1}{2}}^+ + \tilde{S}_{p2,i+\frac{1}{2}}^- = \left[\frac{1}{2}g(h_{2,i-\frac{1}{2}}^+)^2 \right] + \left[-\frac{1}{2}g(h_{2,i+\frac{1}{2}}^-)^2 \right]
\end{aligned} \tag{38}$$

and hence (24) can be rewritten as:

$$(\mathbf{F}_{i+\frac{1}{2}}^* - \mathbf{S}_{i+\frac{1}{2}}^{*-}) - (\mathbf{F}_{i-\frac{1}{2}}^* + \mathbf{S}_{i-\frac{1}{2}}^{*+}) = 0 \tag{39}$$

Therefore, considering a wet-dry configuration for the upper layer at the intercell edge $i + \frac{1}{2}$ defined as:

$$\begin{aligned} h_{1,i} &\neq 0 & h_{1,i+1} &= 0 \\ z_{b,i} + h_{2,i} + h_{1,i} &< z_{b,i+1} \end{aligned} \tag{40}$$

in order to guarantee that the well-balanced property of the numerical scheme is maintained for the upper layer even at wet-dry conditions, it is enough to ensure that:

$$\mathbf{F}_{1,i+\frac{1}{2}}^* - \mathbf{S}_{1,i+\frac{1}{2}}^{*-} = 0 \tag{41}$$

independently of the values of $h_{2,i}$ and $h_{2,i+1}$.

Similarly, considering a wet-dry configuration for the lower layer at the intercell edge $i + \frac{1}{2}$ defined as:

$$\begin{aligned} h_{2,i} &\neq 0 & h_{2,i+1} &= 0 \\ z_{b,i} + h_{2,i} &< z_{b,i+1} \end{aligned} \tag{42}$$

ensuring the well-balance property for the lower layer requires that:

$$\mathbf{F}_{2,i+\frac{1}{2}}^* - \mathbf{S}_{2,i+\frac{1}{2}}^{*-} = 0 \tag{43}$$

independently of the values of $h_{1,i}$ and $h_{1,i+1}$.

The terms $\mathbf{S}_{1,i+\frac{1}{2}}^{*-}$ and $\mathbf{S}_{2,i+\frac{1}{2}}^{*-}$ in (41) and (43) are the integrated source term at the intercell edge $i + \frac{1}{2}$ for the upper and lower layers, respectively, which can be expressed as:

$$\mathbf{S}_{i+\frac{1}{2}}^{*-} = \begin{pmatrix} \mathbf{S}_{1,i+\frac{1}{2}}^{*-} \\ \mathbf{S}_{2,i+\frac{1}{2}}^{*-} \end{pmatrix} = \begin{pmatrix} 0 \\ -\tilde{S}_{p1,i+\frac{1}{2}}^- - \tilde{S}_{\tau1,i+\frac{1}{2}}^- \\ 0 \\ -\tilde{S}_{p2,i+\frac{1}{2}}^- - \tilde{S}_{\tau2,i+\frac{1}{2}}^- \end{pmatrix} \quad (44)$$

250 being $\tilde{S}_{p1,i+\frac{1}{2}}^-$ and $\tilde{S}_{p2,i+\frac{1}{2}}^-$ the integrated pressure terms (38); and $\tilde{S}_{\tau1,i+\frac{1}{2}}^-$ and $\tilde{S}_{\tau2,i+\frac{1}{2}}^-$ the integrated friction term at the left side of the intercell edge $i + \frac{1}{2}$ for the upper and lower layers, respectively, which can be expressed as:

$$\begin{aligned} \tilde{S}_{\tau1,i+\frac{1}{2}}^- &= \frac{1}{2} \left(\frac{\tilde{T}_\omega}{\rho_1} \right)_i \\ \tilde{S}_{\tau2,i+\frac{1}{2}}^- &= -\frac{1}{2} \left(\frac{\tilde{T}_\omega}{\rho_2} \right)_i + \frac{1}{2} \left(\frac{\tilde{T}_b}{\rho_2} \right)_i \end{aligned} \quad (45)$$

4 Reference solutions for two-layer steady flow

A simple method, based on the procedure reported by [16] for steady single-layer
255 flows, is presented in this section to obtain high-accuracy numerical solutions for
1D steady two-layer flow cases. In order to validate the proposed model, reference
solutions obtained with this method for different steady flows are going to be com-
pared with the numerical results obtained for the same flows with the well-balanced
FORCE scheme.

260 Following [16], in steady states $\frac{\partial(\cdot)}{\partial t} = 0$, therefore system (1) can be simplified
to:

$$\begin{aligned}
\frac{dq_1}{dx} &= 0 \\
\frac{d}{dx}\left(\frac{q_1^2}{h_1} + \frac{1}{2}h_1^2\right) &= -gh_1\frac{dz_b}{dx} - gh_1\frac{dh_2}{dx} - \frac{\tau_\omega}{\rho_1} \\
\frac{dq_2}{dx} &= 0 \\
\frac{d}{dx}\left(\frac{q_2^2}{h_2} + g\frac{1}{2}h_2^2\right) &= -gh_2\frac{dz_b}{dx} - gh_2r\frac{dh_1}{dx} + \frac{\tau_\omega}{\rho_2} - \frac{\tau_b}{\rho_2}
\end{aligned} \tag{46}$$

being q_1 and q_2 the flow discharge per unit width of the channel at the upper and lower layers respectively, $q_1 = h_1u_1$ and $q_2 = h_2u_2$. Defining the dimensionless Froude number as $Fr_1 = \sqrt{(q_1^2)/gh_1^3}$ for the upper layer and $Fr_2 = \sqrt{(q_2^2)/gh_2^3}$ for the lower layer, system (46) can be simplified to:

$$\begin{aligned}
\frac{dh_1}{dx}(1 - Fr_1^2) &= -\left(\frac{dz_b}{dx} + \frac{dh_2}{dx}\right) - \frac{\tau_\omega}{gh_1\rho_1} \\
\frac{dh_2}{dx}(1 - Fr_2^2) &= -\left(\frac{dz_b}{dx} + r\frac{dh_1}{dx}\right) + \frac{\tau_\omega}{gh_2\rho_2} - \frac{\tau_b}{gh_2\rho_2}
\end{aligned} \tag{47}$$

Energy equations for both layers can also be obtained with a spatial integration of (47):

$$\begin{aligned}
\frac{dE_1}{dx} &= -\frac{\tau_\omega}{h_1\rho_1} \\
\frac{dE_2}{dx} &= +\frac{\tau_\omega}{h_2\rho_2} - \frac{\tau_b}{h_2\rho_2}
\end{aligned} \tag{48}$$

with:

$$\begin{aligned}
E_1 &= \frac{1}{2}u_1^2 + g(z_b + h_2 + h_1) \\
E_2 &= \frac{1}{2}u_2^2 + g(z_b + rh_1 + h_2)
\end{aligned} \tag{49}$$

Starting from an arbitrary function of the upper layer depth $h_1(x)$, in order to obtain reference solutions for the lower layer depth $h_2(x)$ and the bed elevation $z_b(x)$,

system (47) is solved using an ODE-solver. In this work, the solver *ode45* implemented in Matlab[©] was used to obtain all the exact two-layer steady solutions. It is worthy to note that the reference solutions obtained for $h_2(x)$ and $z_b(x)$ using this method represent high-accuracy numerical approximations to those exact solution.

275 The necessary input flow features for each layer are the densities ρ_1 and ρ_2 , the unit flow discharges q_1 and q_2 , the inlet boundary values for the lower layer depth $h_2(x = 0)$ and bed elevation $z_b(x = 0)$, the friction coefficient at the interface surface $C_{f\omega}$ and the Manning roughness coefficient n_b at the bed surface. The method is summarized on Figure 6.

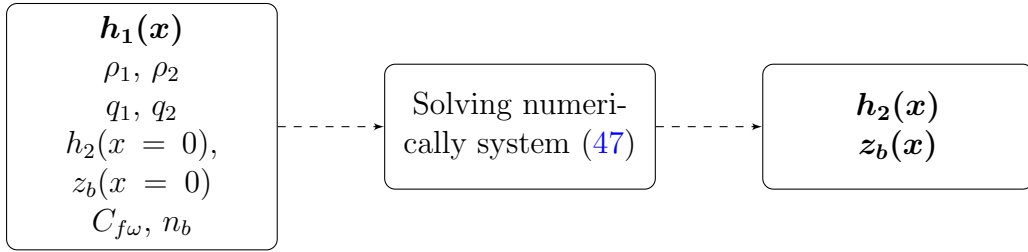


Figure 6: Scheme for the two-layer exact steady solution method.

280 Three steady two-layer flow cases are presented with different density ratios, flow regimes at upper and lower layers and friction coefficients with the purpose of showing cases of interest whose high-accuracy numerical solution has been obtained with the method proposed. All of them consider the spatial domain $0\text{ m} < x < 150\text{ m}$. The upper layer depth function $h_1(x)$ used in all the cases was similar to the one proposed by [16] for the single-layer analytical case:

285

$$h_1(x) = 0.8 + 0.25e^{-33.75(\frac{x}{150} - \frac{1}{2})^2}(m) \quad (50)$$

The required input values for each two-layer steady flow case are shown in Table 1. Case 1 consists of two layers with nearly equal densities ($r = 1/1.15$), with the lower layer under supercritical conditions and the upper layer under subcritical flow regime. Case 2 consists of a two-layer steady flow with both layers under subcritical flow regime and density ratio $r = 1/3$. Both cases 1 and 2 are frictionless at the interface and the bed surfaces. Finally, Case 3 includes a density ratio $r = 1/3$

290

and frictional momentum exchange at the interface and bed surface. The reference solutions obtained for each hypothetical case have been shown and compared with the numerical results in Section 5.2.

Case	ρ_2 (kg/m^3)	ρ_1 (kg/m^3)	q_2 (m^2/s)	q_1 (m^2/s)	$z_b(0)$ (m)	$h_2(0)$ (m)	$C_{f\omega}$ (s^2/m^2)	n_b ($s/m^{1/3}$)
1	1150	1000	1.0	1.0	1.0	0.4	0.0	0.0
2	3000	1000	0.8	1.2	1.0	0.4	0.0	0.0
3	3000	1000	0.4	1.0	1.5	0.4	0.01	0.04

Table 1: Input values for the two-layer steady cases considered.

295

5 Numerical results

In this section, the proposed numerical scheme for the two-layer system is used to solve a set of different problems. Three different conditions are considered in order to validate the numerical behaviour of the proposed scheme: the lake-at-rest
300 benchmarking test, steady flows and highly transient dam-break flows.

5.1 Two-layer lake-at-rest tests

This benchmarking test aims to demonstrate the well-balanced character of the FORCE scheme supplemented with the proposed hydrostatic reconstruction, even including the presence of wet-dry fronts in both layers. Any numerical method is
305 said to be well-balanced if under lake-at-rest conditions, i.e. horizontal free surface and null velocity, no instabilities appear and the static equilibrium is preserved. The hydrostatic reconstruction (3.1) included in FORCE allows the method to fulfil this condition for any value of the parameter α (17) or density ratio r .

A spatial domain $0\,m < x < 100\,m$ is considered with $\Delta x = 1\,m$. Both the bed
310 level z_b and the interface level $z_b + h_2$ are arbitrarily defined as shown in Figure 7, including different wet-dry configurations in both layers. The weighting parameter α is set to 0.5, the CFL and the final simulation textcolorpurpletimes are 0.5 and

2000 s , respectively. Frictionless conditions were also set at the bed and interface surfaces.

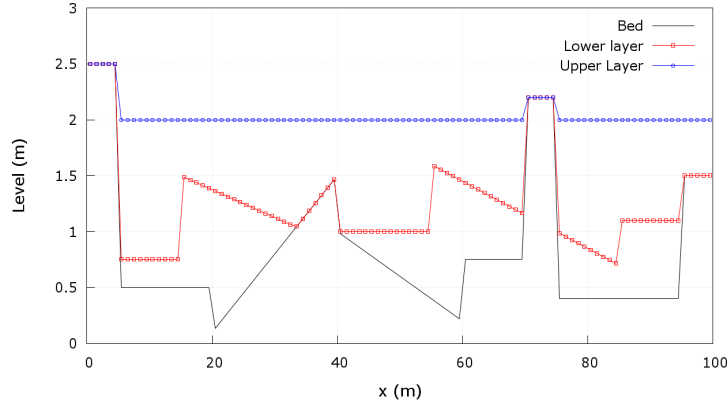


Figure 7: Lake-at-rest initial conditions.

Two cases are considered with different density ratio r between upper and lower layer. First, $r = 1/1$ is set, i.e. two layers of equal density. Figure 8 shows the layer levels and discharges for $t = 2000$ s . Under this condition, the hydrostatic pressure P_2 of the upper layer on the lower layer is exactly balanced by the term P_1 accounting for the variation of the upper layer depth. Therefore, the numerical scheme is able to hold the static equilibrium state without suffering from any perturbation and preserving the initial interface surface unaltered with a horizontal upper layer free surface, as well as null velocities in both layers.

Second, the density ratio between both layers is set to $r = 1/3$, i.e. an upper light fluid over a dense fluid. Under this condition, the hydrostatic pressure P_2 of the upper layer on the lower layer does not balance exactly the upper layer depth variation term P_1 , and hence the initial static equilibrium is lost at the first simulation stages. However, as time progresses, a new static equilibrium state is reached and maintained with horizontal interface levels. Figure 9-top shows the interface and free surface temporal evolution. For the final simulation time $t = 2000$ s the interface and free surfaces are horizontal, and the discharge is null in both layers (Figure 9-bottom).

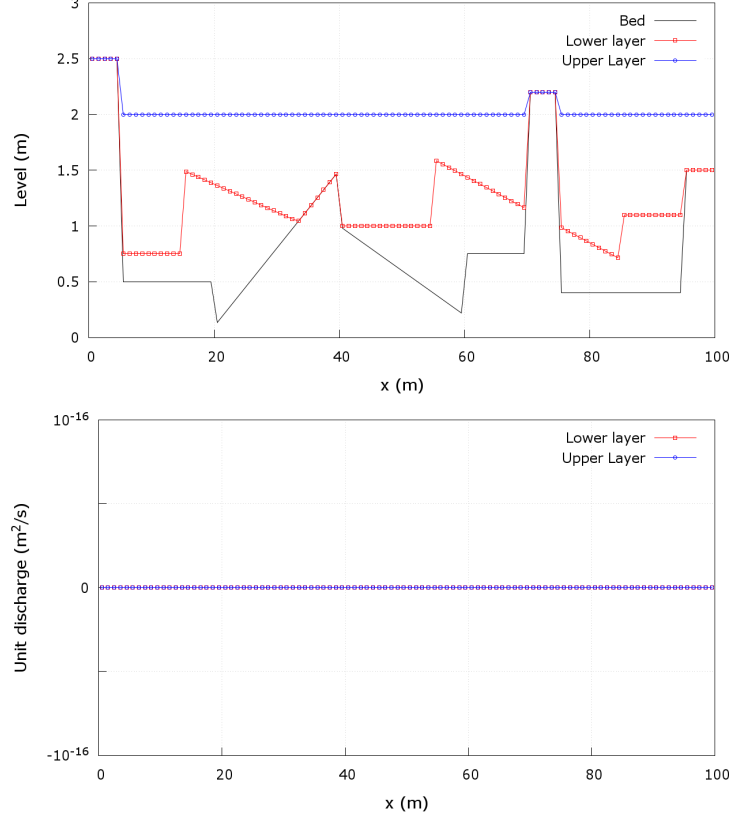


Figure 8: Lake-at-rest with density ratio $r = 1/1$: (top) layer levels at $t = 2000$ s and (bottom) layer discharges at $t = 2000$ s.

5.2 Two-layer steady state tests

In this section, the two-layer steady state cases with reference solution described in Section 4 are simulated using the proposed well-balanced-FORCE scheme. Case 1 and 2 are frictionless with density ratio $r = 1/1.15$ and $r = 1/3$, respectively. Case 3 considers a density ratio $r = 1/3$ and involves friction momentum exchange terms at both the bed surface and the interface surface. The setup parameters for each two-layer steady state case have been reported in Table 1.

A spatial domain $0\text{ m} < x < 150\text{ m}$ is considered with $\Delta x = 1\text{ m}$. The chosen CFL is 0.5 for all the simulations and the weighted parameter α is set to 0.5. At the left boundary cell $x = 0\text{ m}$ a constant discharge is set at both layers, whereas at the right boundary cell $x = 150\text{ m}$ constant values for the layer depths and energies are also imposed. Each simulation is stopped once steady flow regimes are reached at both layers.

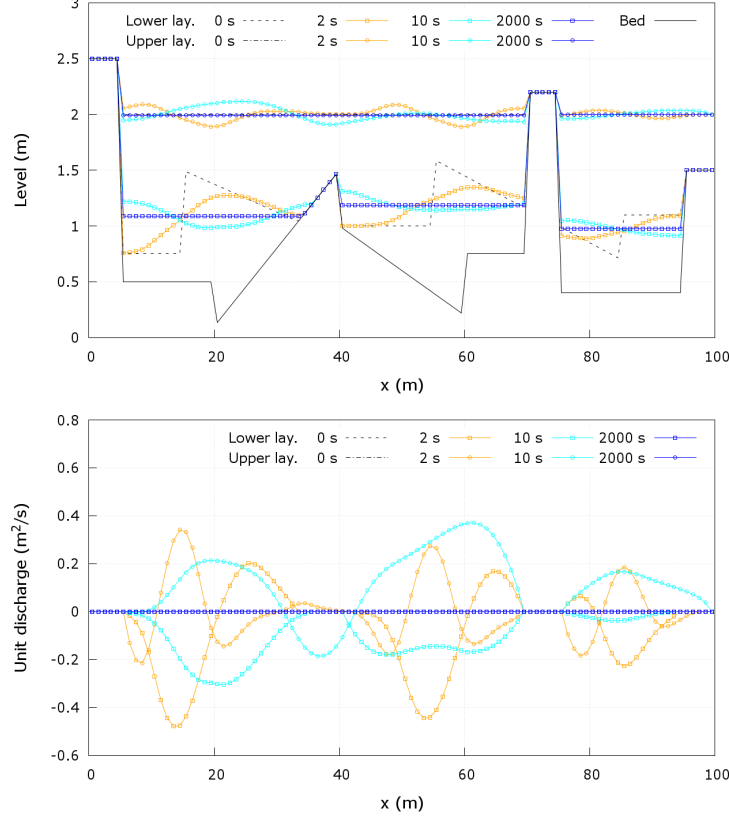


Figure 9: Lake-at-rest with density ratio $r = 1/3$: (top) layer levels temporal evolution and (bottom) layer discharges temporal evolution.

Figure 10 shows the initial condition for Case 1, together with the bed profile and the reference solution for the two-layer steady flow calculated in Section 4. An initial constant elevation is imposed for the interface, as well as for the free surface. Constant discharges $q_2 = 1.0 \text{ m}^2/\text{s}$ and $q_1 = 1.0 \text{ m}^2/\text{s}$ are also imposed at the initial time along the whole spatial domain. The interface friction coefficient C_{fw} is set null, as well as the Manning's roughness coefficient n_b at the bed surface.

For the two-layer steady flow Case 1, numerical instabilities do not appear using the proposed well-balanced FORCE scheme. Figure 11-left depicts the steady numerical interface and free surfaces elevation compared to the reference solution. Although a reasonable agreement is observed for the interface and free surface elevation, some differences appears for the flow velocities (see Figure 11-right), especially in the lower layer.

In order to identify the influence of the mesh discretization, a more refined mesh with $\Delta x = 0.1 \text{ m}$ is also tested. Table 2 shows the root mean square error (RMSE)

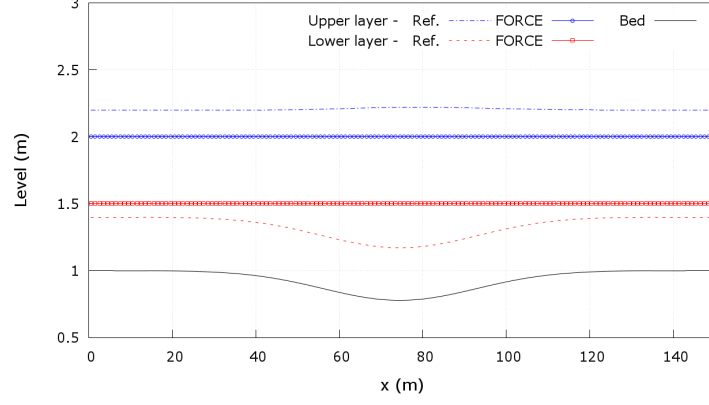


Figure 10: Case 1: Initial condition for the interface and free surfaces, bed profile and reference solution for the two-layer steady flow.

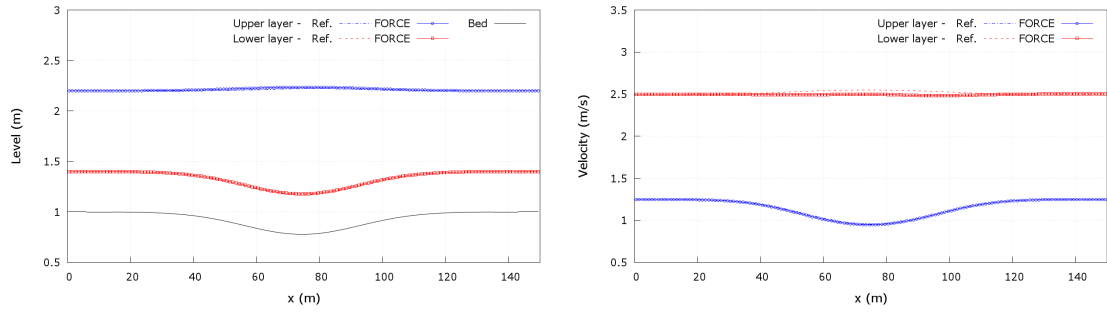


Figure 11: Case 1: comparison of numerical and reference solution for (left) interface and free surface elevations and (right) upper and lower layer velocities.

for the numerical depth (h_1, h_2) and velocities (u_1, u_2) of both layer compared with
 360 the reference solution. The increase in the mesh refinement leads to slightly lower
 errors in all the considered variables, with exception of the lower layer velocity
 u_2 . Furthermore, the influence of the weighting parameter α is also assessed. The
 reduction of $\alpha = 0.1$, maintaining $\Delta x = 1\text{ m}$, reduces the diffusivity of the scheme
 and also leads to slightly lower errors in all the considered variables, with exception
 365 of the lower layer velocity u_2 . However, the mesh refinement is not able to avoid
 the differences in the lower layer velocity between the numerical and the reference
 solutions, neither the reduction of the weighting parameter α .

Figure 12 shows the initial condition, bed profile and reference solution for the
 two-layer steady flow Case 2. Constant elevations are again imposed for both the
 370 interface and the free surfaces. Constant discharges $q_2 = 0.8\text{ m}^2/\text{s}$ and $q_1 = 1.2\text{ m}^2/\text{s}$
 are also imposed at the initial time along the whole spatial domain. The interface

Case 1	h_1 (m)	h_2 (m)	u_1 (m/s)	u_2 (m/s)
$\Delta x = 1\text{ m}$ $\alpha = 0.5$	$4.9 \cdot 10^{-3}$	$4.9 \cdot 10^{-3}$	$6.0 \cdot 10^{-3}$	$2.99 \cdot 10^{-2}$
$\Delta x = 0.1\text{ m}$ $\alpha = 0.5$	$3.7 \cdot 10^{-3}$	$4.9 \cdot 10^{-3}$	$3.9 \cdot 10^{-3}$	$3.09 \cdot 10^{-2}$
$\Delta x = 1\text{ m}$ $\alpha = 0.1$	$4.3 \cdot 10^{-3}$	$4.8 \cdot 10^{-3}$	$4.6 \cdot 10^{-3}$	$3.06 \cdot 10^{-2}$

Table 2: Root mean square errors (RMSE) for Case 1: Influence of the mesh discretization and the weighting parameter α .

friction coefficient $C_{f\omega}$ and the Manning's roughness coefficient n_b at the bed surface are null.

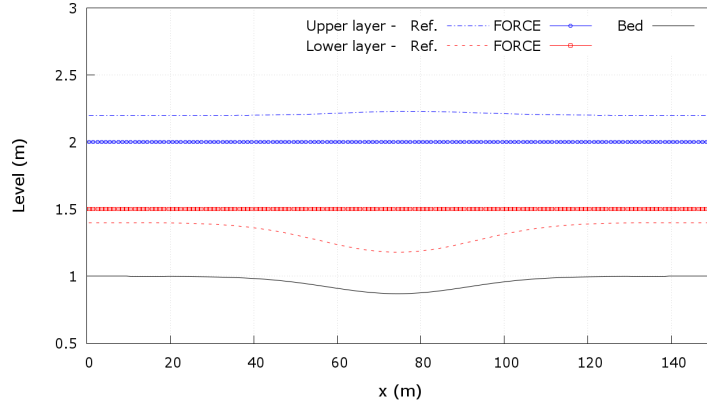


Figure 12: Case 2: Initial condition for the interface and free surfaces, bed profile and reference solution for the two-layer steady flow.

Figure 13-left depicts the steady numerical interface and free surfaces elevation compared to the reference solution. As in the previous case, although a good agreement is observed for the interface and free surface elevation (see Table 3) between the numerical results obtained with the well-balanced FORCE scheme and the high-accuracy solution obtained with the ODE-solver, marked differences appears again in the lower layer flow velocity (see Figure 13-right).

Figure 14 shows the initial condition, bed profile and reference solution for the two-layer steady flow Case 3. As in the previous cases, constant elevations are imposed for both the interface and the free surfaces. Constant discharges $q_2 = 0.4\text{ m}^2/\text{s}$ and $q_1 = 1.0\text{ m}^2/\text{s}$ at the initial time are also imposed. The interface

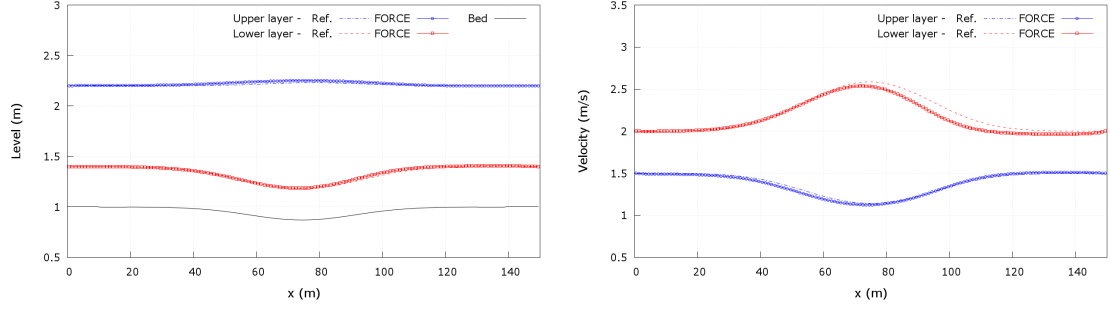


Figure 13: Case 2: comparison of numerical and reference solution for (left) interface and free surface elevations and (right) upper and lower layer velocities.

friction coefficient $C_{f\omega}$ is set to 0.01, whereas the Manning's roughness coefficient
 385 n_b at the bed surface is $0.04 \text{ m s}^{-1/3}$.

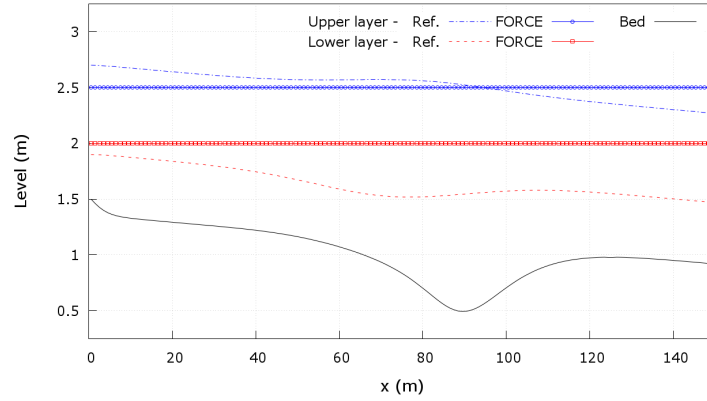


Figure 14: Case 3: Initial condition for the interface and free surfaces, bed profile and reference solution for the two-layer steady flow.

For this two-layer steady flow Case 3, numerical instabilities do not appear either using the proposed well-balanced FORCE scheme, despite of friction terms was included. Figure 15-left shows the steady numerical interface and free surfaces elevation compared to the high-accuracy solution obtained with the ODE-solver, whereas
 390 15-right depicts the flow velocities at both layers. A good agreement is observed for both the interface and free surface elevation, as well as for the flow velocities (see Table 3).

Finally, Table 3 shows the root mean square error (RMSE) in Case 2 and Case 3 with $\Delta x = 1 \text{ m}$ and $\alpha = 0.5$ for the main variables of both layers. The highest
 395 errors occurs for Case 2, specially for the layer averaged velocity u_2 . Case 3 shows lower errors despite it includes the friction dissipation terms.

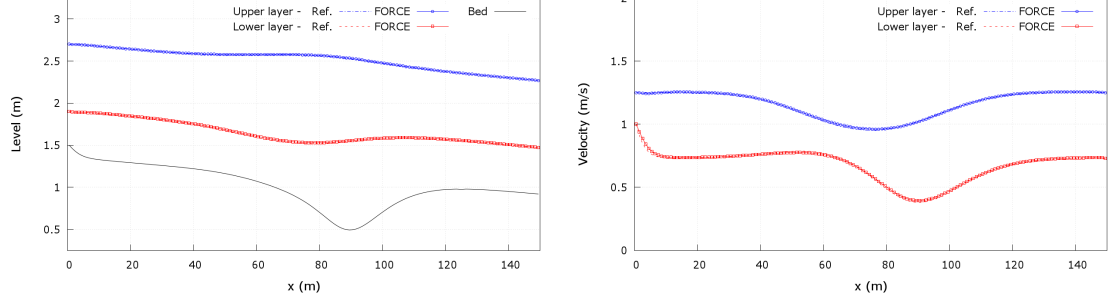


Figure 15: Case 3: comparison of numerical and reference solution for (left) interface and free surface elevations and (right) upper land lower layer velocities.

Test	h_1 (m)	h_2 (m)	u_1 (m/s)	u_2 (m/s)
Case 2	$1.41 \cdot 10^{-2}$	$1.11 \cdot 10^{-2}$	$1.99 \cdot 10^{-2}$	$5.96 \cdot 10^{-2}$
Case 3	$5.50 \cdot 10^{-3}$	$1.02 \cdot 10^{-2}$	$7.2 \cdot 10^{-3}$	$1.03 \cdot 10^{-2}$

Table 3: Root mean square errors (RMSE) for Case 2 and Case 3 with $\Delta x = 1 m$ and $\alpha = 0.5$.

5.3 Two-layer dam-break test

In this section, the proposed well-balanced FORCE scheme for two-layer flows is faced to a theoretical dam-break case. Dam-break is a highly transient benchmarking test widely used for validation of shallow water numerical methods. In order to be able to use the single-layer analytical solution for comparison, the density ratio r is set to $1/1.15$, i.e. both fluids with approximately the same density. A spatial domain $-100 m < x < 100 m$ is considered with $\Delta x = 1 m$. The final simulation time is $15 s$, the CFL condition is set to 0.5 and the parameter α is equal to 0.25 . Friction terms are null at the bed and interface surfaces. Both layers are set initially at rest, with a sharp discontinuity at $x = 0 m$ for the upper layer depth:

$$h_1(x) = \begin{cases} 1.5 \text{ m} & \text{if } x \leq 0.0 \text{ m} \\ 0.5 \text{ m} & \text{if } x > 0.0 \text{ m} \end{cases} \quad h_2(x) = \begin{cases} 0.5 \text{ m} & \text{if } x \leq 0.0 \text{ m} \\ 0.5 \text{ m} & \text{if } x > 0.0 \text{ m} \end{cases} \quad (51)$$

Figure 16 shows the numerical results for the interface and free surface levels at $t = 5 s$, $t = 10 s$ and $t = 15 s$. The exact solution for the single-layer free

surface level has also been plotted. As the densities of the upper and lower fluids
 410 are approximately equal, the free surface level evolution agrees with the exact single-
 layer solution, despite of a marked change appearing at the interface surface. The
 dambreak shock wave going to the right direction moves with the same velocity as
 the single-layer exact solution. Furthermore, also the rarefaction wave going to the
 left direction agrees in height and velocity with the exact solution.

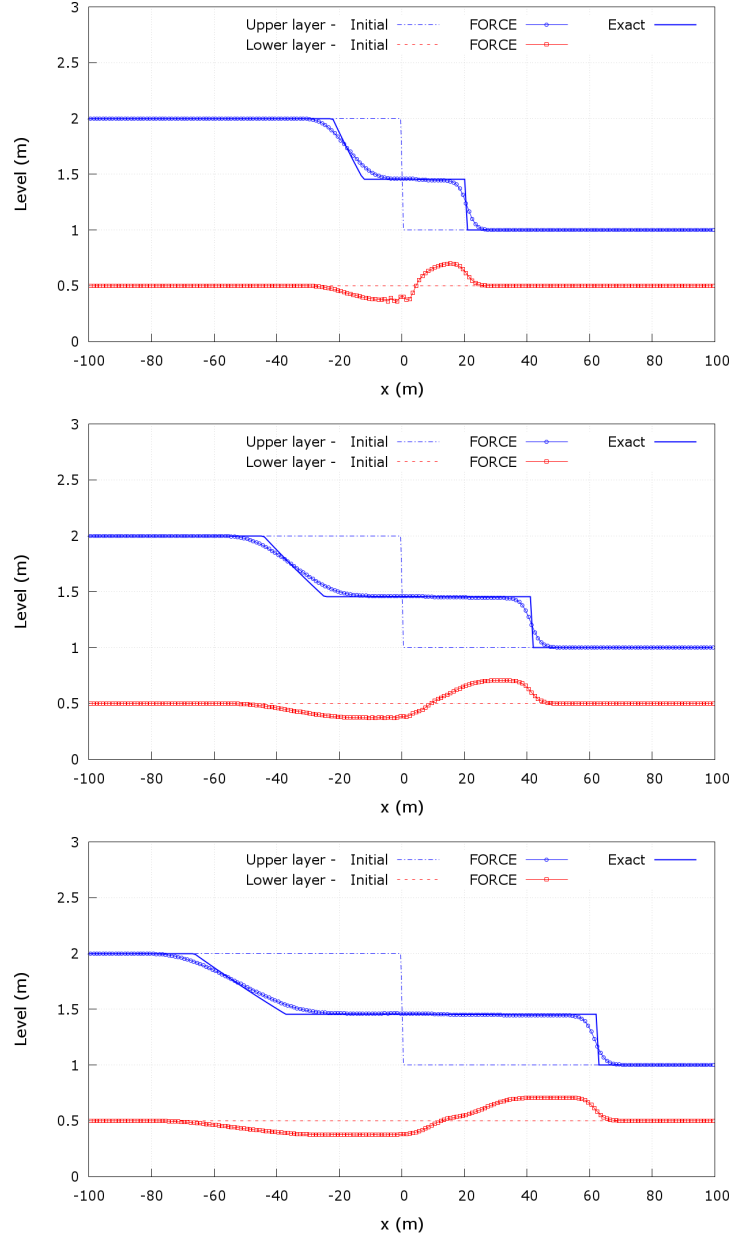


Figure 16: Dam-break temporal evolution with $r = 1/1.15$ and $\alpha = 0.25$: (top) $t = 5 s$, (center) $t = 10 s$ and (bottom) $t = 15 s$.

415 In order to analyse the effects of the density ratio variations, the idealised

dambreak test case is also simulated considering $r = 1/1$, i.e. both fluid with exactly the same density, and $r = 1/3$ accounting for a light fluid over a dense layer. Figure 17 shows the numerical results for the interface and free surface levels at $t = 5\text{ s}$, $t = 10\text{ s}$ and $t = 15\text{ s}$. On one hand, for $r = 1/1$ numerical instabilities appear at the initial discontinuity region in the interface between both layers and they propagate as the dambreak progresses. These instabilities do not disappear when reducing the CFL as they are a consequence of the loss of the hyperbolic character of the mathematical system [3]. However, as the density of both fluid is equal, these oscillations do not affect the free surface, which agrees with the exact single-layer solution. On the other hand, when the density ratio between layers is $r = 1/3$, the level changes in the interface are less marked as the pressure term of the upper layer over the lower layer P_2 is reduced. In this case, the numerical solution is more stable. The free surface evolution cannot be compared with the exact solution for the single-layer problem in this case.

In order to analyse the effects of the weighted parameter α on the stability and accuracy of the proposed numerical scheme, the same dambreak test case is simulated considering $r = 1/3$ and varying $\alpha = 0.5$, $\alpha = 0.1$ and $\alpha = 0$. As shown in Figure 18, values of α near to 0.5 lead to diffusive solutions, as the first order Lax-Friedrich flux dominates the numerical flux computation. When α is reduced to 0.1, the Lax-Wendroff formulation, which is second order in time and space, has a more marked influence on composed numerical FORCE flux and hence the solution becomes less diffusive. Nevertheless, when α is exactly 0 a predictable oscillatory behaviour was observed in the solution, derived from the pure second order Lax-Wendroff formulation.

Finally, to demonstrate the capability of the well-balanced FORCE scheme to deal with two-layer flow configuration which causes loss of hyperbolicity of the coupled system, the idealized dambreak with $r = 1/1$ is analyzed. This case shows complex eigenvalues of the coupled Jacobian matrix [21], which make difficult the computation of the problem based on the coupled Jacobian. With the well-balanced

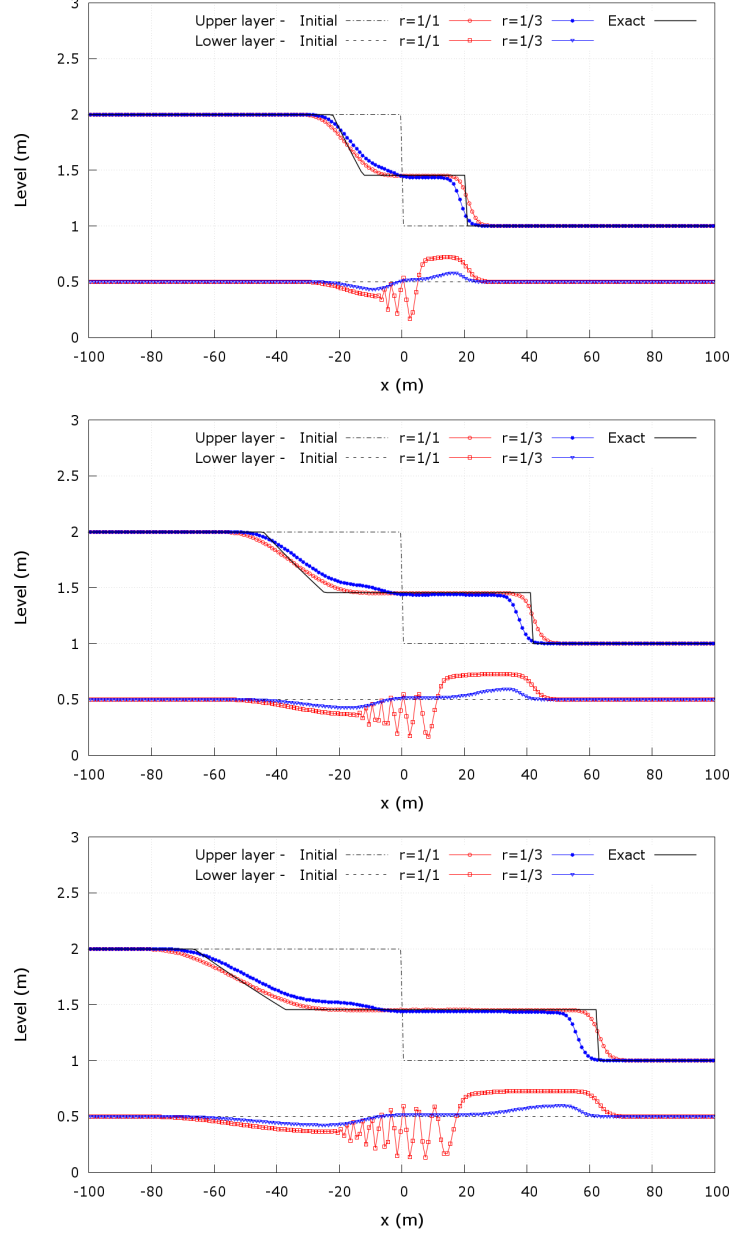


Figure 17: Dam-break temporal evolution for $r = 1/1$ and $r = 1/3$, with $\alpha = 0.25$: (top) $t = 5\text{ s}$, (center) $t = 10\text{ s}$ and (bottom) $t = 15\text{ s}$.

445 FORCE scheme, numerical oscillations appear at the interface since the beginning and remain afterward (see Figure 17), but the scheme remains stable for the free surface computation without showing a dramatic crash.

Furthermore, although it is not possible to totally avoid these oscillations, their amplitude can be controlled by increasing the diffusivity of the scheme. The most effective way to increase the numerical diffusivity is to decrease the CFL. The undesirable effects of lower CFL numbers on the solution accuracy can be partially

450

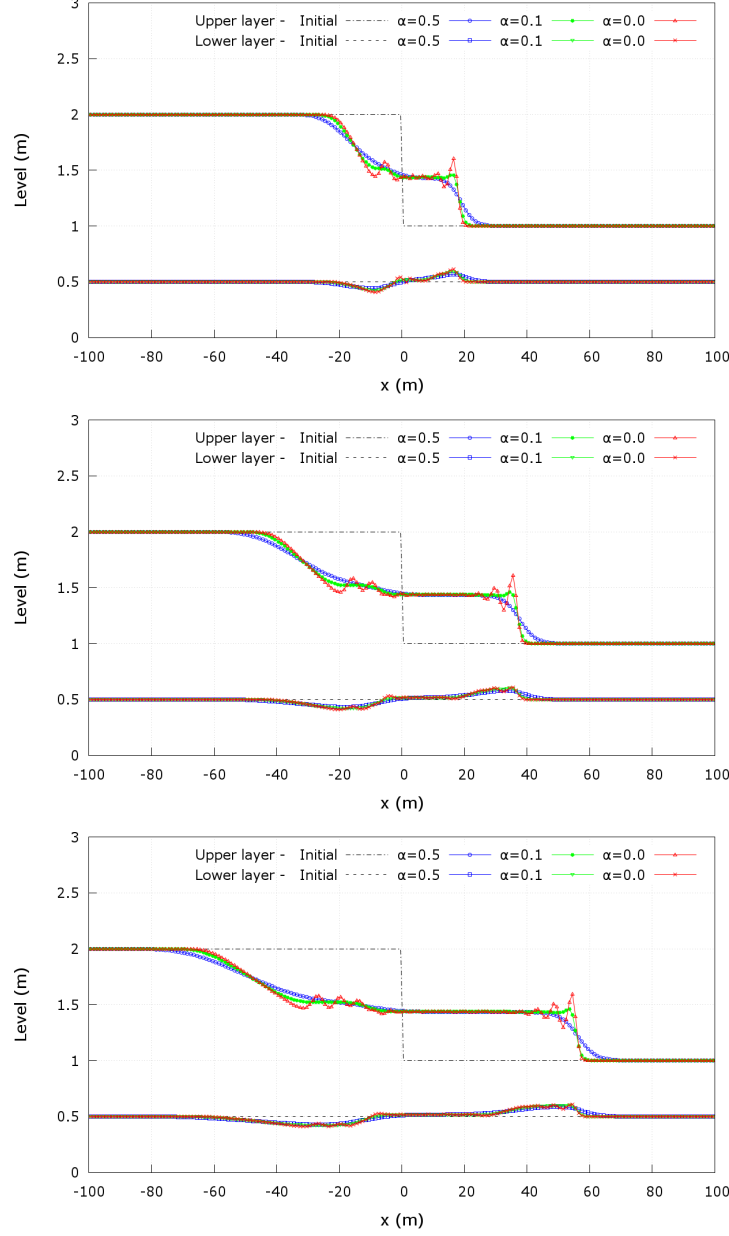


Figure 18: Dam-break temporal evolution with $r = 1/3$ and $\alpha = 0.5 - \alpha = 0.1 - \alpha = 0$: (top) $t = 5 s$, (center) $t = 10 s$ and (bottom) $t = 15 s$.

corrected by tuning the weighting parameter α . Figure 19 shows the dambreak temporal evolution with $r = 1/1$, CFL=0.1 and $\alpha = 0.05$ on the left. Also the eigenvalues of the coupled Jacobian matrix have been plotted on the right to show that this case corresponds to a situation in which loss of hyperbolicity exits. Comparison with Figure 17 shows that the numerical oscillations amplitude is reduced at the interface and the free surface is accurately predicted.

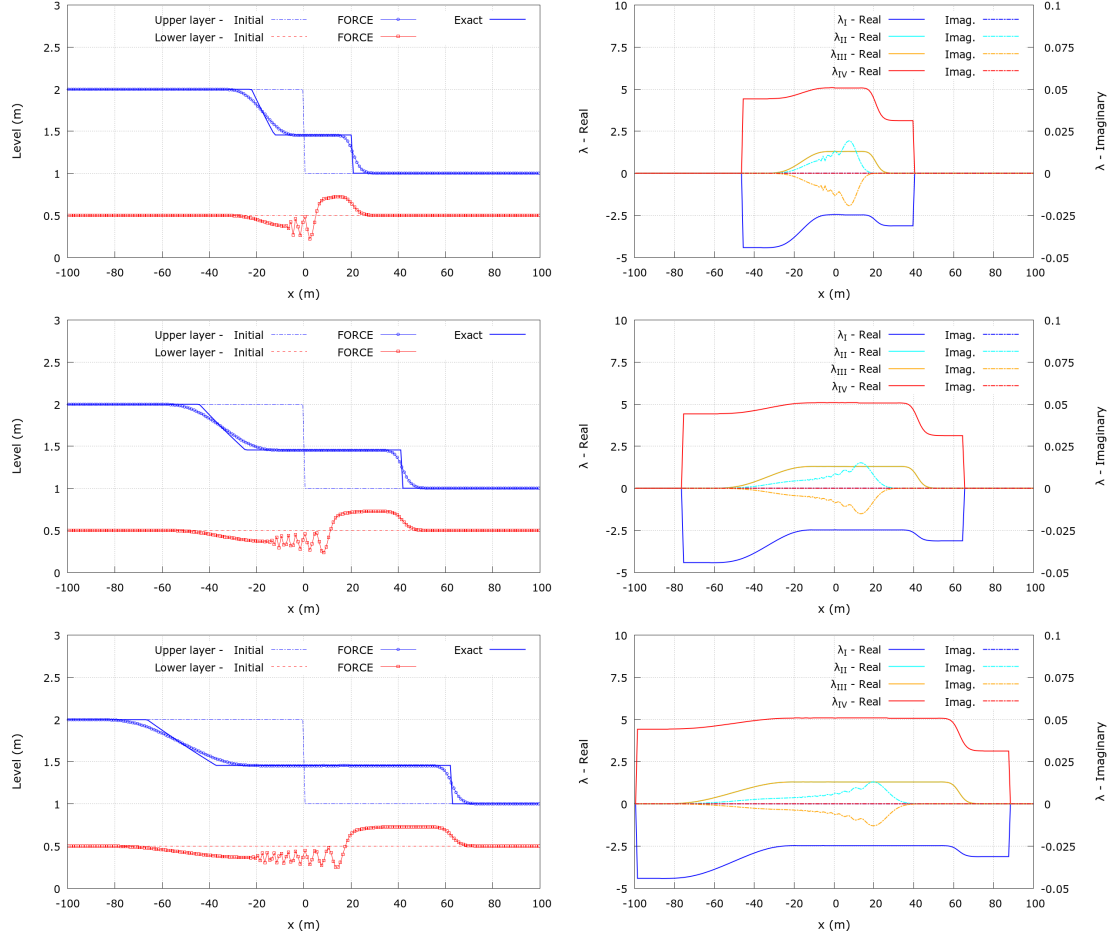


Figure 19: Dam-break temporal evolution with $r = 1/1$, $CFL=0.1$ and $\alpha = 0.05$: (left column) free surface and interface evolution, (right column) eigenvalues of the coupled Jacobian matrix.

5.4 Experimental dam-break over movable bed

The proposed scheme is tested against a laboratory case consisting of a water dam-break over a flat movable bed. This experimental test [31] consists of an idealised
460 dam-break flow over a sediment flat bed made of sand with grain diameter 1.82 mm , density $\rho = 2683\text{ kg/m}^3$ and porosity $p = 0.47$. The experiment was carried out in a 6 m long and 0.25 m wide flume. The thickness of the sand layer was 5 cm over the flume floor. Breaking of the dam was reproduced by the downward movement of a
465 pneumatically actuated thin gate placed at the middle of the flume. The initial water level was 0.35 m upstream the gate and nil downstream. The temporal evolution of the free surface and bed surface were reported experimentally until 1.5 s after the gate opening each 0.25 s .

The simulations have been performed with a cell size $\Delta x = 0.01\text{ m}$, $\text{CFL} = 0.1$ and $\alpha = 0.5$. The turbulent friction term at the interface between the upper layer (water) and the lower layer (sand bed) is approximated using a variable friction coefficient $C_{f\omega} = n_\omega^2/h_1^{1/3}$, being $n_\omega = 0.018\text{ m s}^{-1/3}$ a Manning-type roughness coefficient. The friction term between the sand layer and the flume floor is computed using a Chézy-type formulation, $\tau_b = \rho_2 g C_{fb} u_2 |u_2|$, being $C_{fb} = 0.1\text{ s}^2/\text{m}$. The upper layer density was $\rho_1 = 1000\text{ kg/m}^3$, whereas the bulk density of the sand layer is estimated as $\rho_2 = 1892\text{ kg/m}^3$.

Figure 20-left shows the numerical results for the temporal evolution of the water free surface and bed level. The experimental results have been also plotted for comparison. In general, a good agreement with measured data can be found for all the times reported. The free water surface and the bed level are well predicted and the propagation velocity of the dam-break wave is accurately captured. Furthermore, the temporal evolution of the velocity in both layer has been also plotted in Figure 20-right. The upper layer velocity maximum increases progressively as the dam-break wave progressed downstream the flume, whereas the lower layer averaged velocity remains stable along the dam-break flow.

6 Conclusions

This work demonstrates the possibility of simulating two-layer shallow flows with well-balanced FORCE schemes. In order to ensure this property, a new hydrostatic reconstruction procedure has been also proposed which ensures a correct balance between the homogeneous fluxes and the source terms at the intercell edges even under wet-dry conditions. Furthermore, in order to obtain new benchmarking tests for steady two-layer flows, a pioneering method to obtain high-accuracy reference solutions has been reported. This method allows to consider in the reference solution the dissipation terms caused by the frictional effects at both the interface separating fluid layers and the bed surface.

The numerical scheme has been tested against steady and transient two-layer

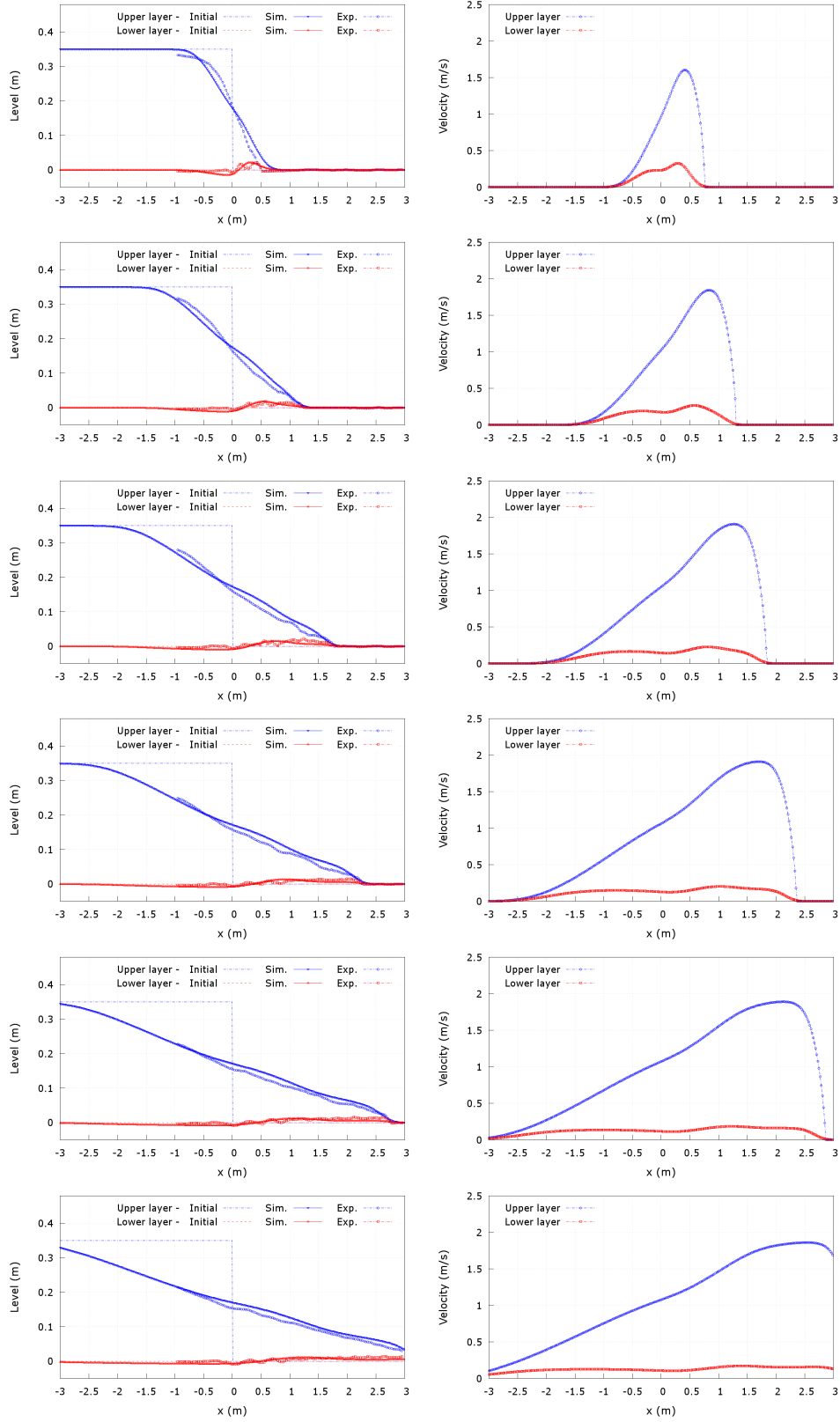


Figure 20: Experimental dambreak over movable bed: (left) free surface and bed levels and (right) upper and lower layer velocities. From top to bottom, $t = 0.25\text{ s}$, $t = 0.50\text{ s}$, $t = 0.75\text{ s}$, $t = 1\text{ s}$, $t = 1.25\text{ s}$ and $t = 1.5\text{ s}$.

cases. First the FORCE scheme supplemented with the hydrostatic reconstruction has been faced to the lake-at-rest test considering different density ratios r between fluids and wet-dry configurations in both layers. The model is able to reach equilibrium states regardless of the value of r imposed, proving the well-balance property of the scheme. Then, the FORCE model has been tested against three different two-layer steady flow cases with reference solution, which have been obtained by means of the proposed high-accuracy numerical procedure and including different flow regimes, density ratios and friction terms. The numerical results show a good agreement with the reference solutions for the three steady cases and avoiding the appearance of numerical instabilities. The numerical scheme has also been applied to a two-layer dam-break test, considering different density ratios. The sensitivity of the FORCE scheme to the value of r has been analysed. Generally, the model becomes more stable as the density ratio decreases, i.e. as the lower layer increases its density respect to that of the upper layer. When the density ratio between layers is $r = 1/1$ the mathematical two-layer coupled system loses its hyperbolic character. However, this method is able to deal with the instabilities associated by increasing the numerical viscosity. The effects of the weighting parameter α , balancing the first order Lax-Friedrichs flux and the second order Lax-Wendroff flux at the cell edges, has also been studied. Results demonstrate that values of α smaller than the typical value $\alpha = 0.5$ are enough to avoid the oscillatory character of the pure Lax-Wendroff formulation and to reduce the excessive numerical diffusion associated to the Lax-Friedrichs scheme. Finally, the proposed scheme has been tested against an experimental dam-break over movable flat bed case, involving the advance of a wet-dry front. The scheme is able to predict with a reasonable accuracy the free surface evolution and the movable bed changes. The obtained results show the big potential of FORCE scheme, supplemented with the proposed hydrostatic reconstruction method, to be used as modelled tool on real two-layer shallow-flow applications.

525 **Acknowledgements**

This work was developed under a CSIC-JAE grant in the framework of the project PGC2018-094341-B-I00, which is funded by MINECO/FEDER and by Diputacion General de Aragon, DGA, through Fondo Europeo de Desarrollo Regional, FEDER.

References

- 530 [1] Alexander Kurganov and G Petrova. Central-upwind schemes for two-layer shallow water equations. *SIAM J. Scientific Computing*, 31:1742–1773, 01 2009.
- [2] Benoit Spinewine, Vincent Guinot, Sandra Soares-Frazão, and Yves Zech. Solution properties and approximate riemann solvers for two-layer shallow flow models. *Computers & Fluids*, 44(1):202 – 220, 2011.
- 535 [3] M.J. Castro-Díaz, C. Parés-Madroñal, E.D. Fernández-Nieto, and J.M. González-Vida. Numerical treatment of the loss of hyperbolicity of the two-layer shallow-water system. *Journal of Scientific Computing*, 48(1-3):16–40, 2011.
- [4] Laurence Armi. The hydraulics of two flowing layers with different densities.
540 *Journal of Fluid Mechanics*, 163:27–58, 1986.
- [5] K.H. Ardron. One-dimensional two-fluid equations for horizontal stratified two-phase flow. *International Journal of Multiphase Flow*, 6(4):295 – 304, 1980.
- [6] Su-Chin Chen and Szu-Hsien Peng. Two-dimensional numerical model of two-layer shallow water equations for confluence simulation. *Advances in Water*
545 *Resources*, 29(11):1608 – 1617, 2006.
- [7] F. Bouchut and T.M. de Luna. An entropy satisfying scheme for two-layer shallow water equations with uncoupled treatment. *Mathematical Modelling and Numerical Analysis*, 4:683, 2008.
- [8] R. Abgrall and S. Karni. Two-layer shallow water system: A relaxation ap-
550 proach. *SIAM journal of scientific computing*, 3:1603, 2010.
- [9] Alexandre Chiapolino and Richard Saurel. Models and methods for two-layer shallow water flows. *Journal of Computational Physics*, 05 2018.

- [10] Kyle T. Mandli. A numerical method for the two layer shallow water equations with dry states. *Ocean Modelling*, 72:80 – 91, 2013.
- 555 [11] J.B. Schijf and J.C. Schönfeld. Theoretical considerations on the motion of salt and fresh water. *Proceedings Minnesota International Hydraulic Convention*, 01 1954.
- [12] D.M. Farmer and L. Armi. Maximal two-layer exchange over a sill and through the combination of a sill and contraction with barotropic flow. *Journal of Fluid*
560 *Mechanics*, 164(10):53–76, 1986.
- [13] Nino Krvavica, Ivica Kožar, Vanja Travaš, and Nevenka Ožanić. Numerical modelling of two-layer shallow water flow in microtidal salt-wedge estuaries: Finite volume solver and field validation. *Journal of Hydrology and Hydromechanics*, 65(1):49 – 59, 2017.
- 565 [14] Armando Balloffet and Deva K. Borah. Lower mississippi salinity analysis. *Journal of Hydraulic Engineering*, 111(2):300–315, 1985.
- [15] E.F Toro. On glimm-related schemes for conservation laws. technical report mmu-9602. Technical report, Department of Mathematics and Physics, Manchester Metropolitan University, UK, 1996.
- 570 [16] MacDonald Ian. *Analysis and computation of steady open channel flow*. Department of Mathematics. The University of Reading, 1996.
- [17] Toro E. F. *Riemann Solvers and Numerical Methods for Fluid Dynamics: a Practical Introduction*. Springer Berlin / Heidelberg, 1997.
- [18] Naef D., Rickenmann D., Rutschmann P., and McArdell B. W. Comparison of
575 flow resistance relations for debris flows using a one-dimensional finite element simulation model. *Nat. Hazards Earth Syst. Sci*, 2006.
- [19] R. Manning. On the flow of water in open channels and pipes. *Institute of Civil Engineers of Ireland*, 1890.

- [20] C. Swartenbroekx, Y. Zech, and S. Soares-Frazão. Two-dimensional two-layer
580 shallow water model for dam break flows with significant bed load transport.
International Journal for Numerical Methods in Fluids, 2013.
- [21] Nino Krvavica, Miran Tuhtan, and Gordan Jelenić. Analytical implementation
of roe solver for two-layer shallow water equations with accurate treatment for
loss of hyperbolicity. *Advances in Water Resources*, 122:187 – 205, 2018.
- 585 [22] Nino Krvavica. Re-evaluating efficiency of first-order numerical schemes for
two-layer shallow water systems by considering different eigenvalue solutions.
Advances in Water Resources, 137:103508, 2020.
- [23] Michael Dumbser, Arturo Hidalgo, Manuel Castro, Carlos Parés, and Eleu-
terio F. Toro. Force schemes on unstructured meshes ii: Non-conservative
590 hyperbolic systems. *Computer Methods in Applied Mechanics and Engineering*,
199(9):625 – 647, 2010.
- [24] E.F. Toro and S.J. Billett. Centred TVD schemes for hyperbolic conservation
laws. *IMA Journal of Numerical Analysis*, 20(1), 2000.
- [25] Eleuterio F. Toro, Arturo Hidalgo, and Michael Dumbser. Force schemes on
595 unstructured meshes i: Conservative hyperbolic systems. *Journal of Computa-
tional Physics*, 228(9):3368 – 3389, 2009.
- [26] Peter D. Lax. Weak solutions of nonlinear hyperbolic equations and their
numerical computation. *Communications on Pure and Applied Mathematics*,
7(1):159–193, 1954.
- 600 [27] Peter Lax and Burton Wendroff. Systems of conservation laws. *Communications
on Pure and Applied Mathematics*, 13(2):217–237, 1960.
- [28] Carlos S. Kubrusly Carlos A. de Moura. *The Courant–Friedrichs–Lewy (CFL)
Condition, 80 Years After Its Discovery*. Extras Springer. Birkhäuser, 2013.

- [29] Emmanuel Audusse, François Bouchut, Marie-Odile Bristeau, Rupert Klein,
605 and Benoit Perthame. A fast and stable well-balanced scheme with hydrostatic
reconstruction for shallow water flows. *Siam Journal on Scientific Computing*,
25, 01 2004.
- [30] A. Mahdavi and N. Talebbeydokhti. Modeling of non-breaking and breaking
solitary wave run-up using FORCE-MUSCL scheme. *Journal of hydraulic re-*
610 *search*, 4:476, 2009.
- [31] B. Spinewine and Y Zech. Small-scale laboratory dam-break waves on movable
beds. *Journal of Hydraulic Research*, 45(sup1):73–86, 2007.